Estimating Bulk-Composition-Dependent H_2 Adsorption Energies on Cu_xPd_{1-x} Alloy (111) Surfaces

Jacob R. Boes, Gamze Gumuslu, James B. Miller, Andrew J. Gellman, and John R. Kitchin*

Department of Chemical Engineering, Carnegie Mellon University, 5000 Forbes Avenue, Pittsburgh, Pennsylvania 15213, United States

ⓢ Supporting Information

ABSTRACT: The bulk-composition-dependent dissociative adsorption energy of hydrogen on CuPd alloys has been measured experimentally and modeled using density functional theory. The hydrogen adsorption energy cannot be simply defined by a single reactive site or as a composition weighted average of the pure metal components. We developed a modeling approach that uses a basis of active sites weighted by a model site probability distribution to estimate a bulk-composition-dependent adsorption energy. The approach includes segregation under reaction conditions. With this method, we can explain the composition-dependent adsorption energy of hydrogen on Cu-rich alloy surfaces. In Pd-rich alloys, a Pd-hydride phase may form, which results in deviations from trends on the metallic alloy surface.

KEYWORDS: density functional theory, active site, segregation, reaction conditions, palladiumhydride, Vegard's law, Gibbs isotherm
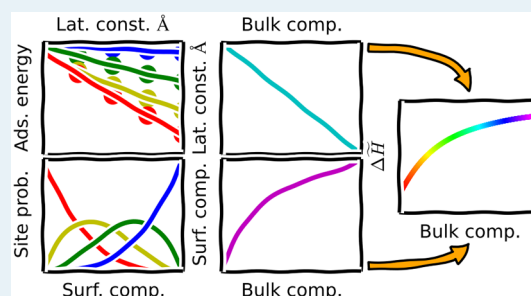
1. INTRODUCTION

Alloys are frequently used as catalysts because they can be designed with properties superior to those of their parent materials.[1] Computational catalysis has made many contributions to understanding the reactivity of alloy active sites for designing such superior catalysts; however, computational methods can be incorporated into catalyst design only when the structure and composition of the sites are known.[2] Under these circumstances, we can readily estimate the reactivity of a site.[3,4] Several significant challenges remain when modeling alloy catalysts. A real alloy surface will have a distribution of sites with different compositions and possible structures, each with its own properties. In addition, the composition of an alloy surface is not likely to be the same as that of the bulk alloy because of segregation effects.[5] Furthermore, the surface composition may depend on the gas-phase environment.[6] Thus, although we can model the properties of a single site, or even many sites, identifying *which* site(s) to model and how significant they are under reaction conditions remains a challenge. Furthermore, if there are multiple sites, it is challenging to determine the properties of the ensemble of sites.

In typical studies of adsorption on alloy surfaces, specific site structures and compositions are modeled.[7,8] These studies are valuable, but they can be difficult to connect directly to experiments because the compositions modeled are often not the same as the experimental compositions, for example, because of segregation effects. Although there are growing efforts experimentally to measure segregation profiles at clean alloy surfaces[9,10] and computational databases of segregation energies exist,[11,12] these results may have limited value under reaction conditions when adsorbate-induced segregation has been observed.[6,13,14] State of the art modeling of alloy surfaces that incorporates segregation from the bulk, adsorption on the surface, and the reactive conditions relies either on atomistic thermodynamic approaches[6] or cluster expansion and Monte Carlo methods.[15,16] Both of these methods, although thermodynamically rigorous, are very computationally demanding. A simpler, more efficient approach is needed to enable better comparison of experiment and computation.

In this manuscript, we illustrate a simple method to model adsorption behavior on heterogeneous alloy surfaces using density functional theory (DFT) and statistical models. In this method, we define a basis of adsorption sites that are likely to span the types of sites that will have the greatest impact on the adsorption energy. For each site, dissociative adsorption energies are then related to bulk composition using a relatively small set of DFT calculations. The probability of finding each active site at the surface is determined through a statistical distribution dependent on an arbitrary surface composition. The effective adsorption energy is then the sum of each site's adsorption energy times its probability of appearing on the surface. Finally, the surface composition is calculated by relating the Langmuir–McLean formulation of the Gibbs free isotherm to the experimentally determined vacuum segregation energy and an estimation of the segregation due to adsorbates.

The surface composition is estimated using experimental segregation data in conjunction with the calculated adsorption

energies to estimate the surface composition under reaction conditions. Finally, the distribution of active sites is estimated from the surface composition and used to weight the calculated adsorption energies into the effective adsorption energy for the surface.

To illustrate this method, we look specifically at the CuPd system that has been well studied experimentally due to its application as an extremely selective separator of H_2 gas from syngas streams.[17−19] We prepared a composition spread alloy film (CSAF)[20] mapping out the CuPd bulk composition space and determined the adsorption energy of H_2 as a function of bulk composition through analysis of H_2−D_2 exchange kinetics. We then compare our computationally estimated bulk-composition-dependent adsorption energies with these experimental results. Through this comparison, we show that the method provides a reasonable approach for predicting chemical properties across bulk composition space. By studying deviations in adsorption energy predictions from those measured, the method also allows for a more detailed understanding of the surface characteristics at the atomic level.

2. METHODS

2.1. Experimental Methods. We measured H_2−D_2 exchange kinetics across $Cu_xPd_{1−x}$ composition space using composition spread alloy film (CSAF) combinatorial materials libraries (shown schematically in Figure 1). CSAFs are thin
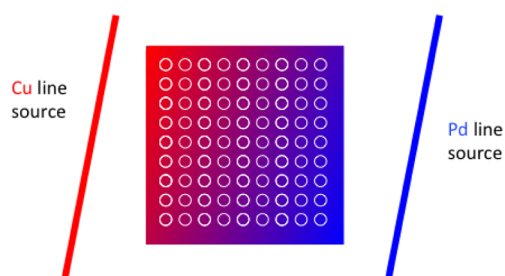

Figure 1. Schematic representation of a $Cu_xPd_{1−x}$ CSAF. Cu (red) and Pd (blue) line sources are shown at the sides of the CSAF. Circles represent a 10×10 grid of microreactors distributed across the surface of the CSAF for kinetic measurements.

alloy films with continuously variable lateral composition that are deposited onto compact substrates. We have previously reported the preparation and characterization of the CuPd CSAFs used in this work.[21] Briefly, an offset filament source[10,22] was used to deposit films of CuPd that are ~100 nm thick, with composition ranging from $x = 0.3$ to 1.0, onto the surfaces of 14 mm × 14 mm × 2 mm polycrystalline Mo substrates; Figure 1 is a schematic diagram of the CSAF. After annealing the CSAF at 800 K, we used a unique multichannel microreactor[23] to measure the kinetics of H_2−D_2 exchange at 100 discrete locations on the CSAF surface (indicated by the circles in Figure 1) over a temperature range of 300−600 K and at various flow rates.

We previously reported a microkinetic model that we developed for interpretation of H_2−D_2 exchange data.[18] The model is based on two elementary steps: dissociative adsorption of H_2 (D_2, HD) and recombinative desorption of H and D atoms to form HD (H_2, D_2). The model consists of a mass balance and a microkinetic expression for the rate of HD formation. We fit the model to the reaction data collected at each of the 100 locations on the surface of the CSAF to extract

estimates of the adsorption ($\Delta E_{ads}^{\ddagger}$) and desorption ($\Delta E_{des}^{\ddagger}$) barriers. The adsorption energy is simply the difference between these two quantities ($\Delta E_{ads}^{H_2} = \Delta E_{des}^{\ddagger} - \Delta E_{ads}^{\ddagger}$).

2.2. Computational Methods. All calculations were performed using the Vienna ab initio simulation package (VASP)[24,25] with the Perdew−Burke−Ernzerhof generalized gradient approximation (GGA−PBE)[26,27] exchange-correlation functional. Core electrons were described using the projector augmented wave function (PAW).[28,29] k-Points were represented using Monkhorst−Pack grids,[30] and the Kohn−Sham orbitals were expanded up to energy cutoffs of 425 eV for CuPd alloy models and 450 eV for PdH models. The Methfessel−Paxton scheme was used with a smearing parameter of 0.4 eV.[31] All calculations involving relaxations were completed with a force criteria <0.05 eV/Å. Pure component lattice constants were determined using bulk calculations with $12 \times 12 \times 12$ k-point grids. Hydride bulk calculations were performed with $8 \times 8 \times 8$ k-point grids. Convergence studies of hydrogen adsorption energies computed with these parameters suggest the results are converged within ±0.02 eV.

Alloy slab calculations were completed with $8 \times 8 \times 1$ k-point grids. The slab geometries were constructed with four metal layers, in which the bottom two layers were fixed in place using various lattice constants between those of the pure components: 3.631 Å for Cu and 3.952 Å for Pd. The remaining two layers and the adsorbate were allowed to relax in the z-axis. Hydride slabs were modeled as symmetric cells with a total of six metal layers, Pd-terminated. The two center layers were fixed in place while the remaining two layers on either side were allowed to relax in the z-axis. A $10 \times 10 \times 1$ k-point grid was used for these calculations. All slab geometries include 10 Å of vacuum in the z-axis. An extensive listing of all computational details is provided in the Supporting Information file.

3. RESULTS AND DISCUSSION

3.1. Experimental Determination of Effective Adsorption Energies. The measured adsorption ($\Delta E_{ads}^{\ddagger}$) and desorption ($\Delta E_{des}^{\ddagger}$) barriers are shown in Figure 2 over a large span of bulk compositions. Dissociative adsorption
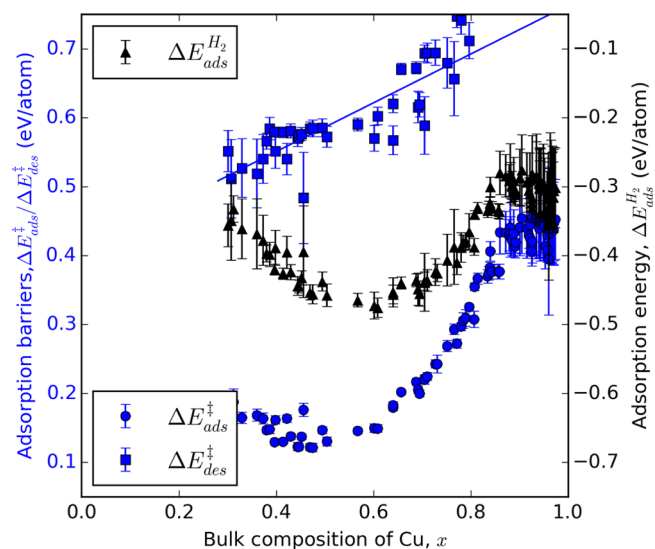

Figure 2. Experimental adsorption ($\Delta E_{ads}^{\ddagger}$) and desorption ($\Delta E_{des}^{\ddagger}$) barriers. Black triangles represent adsorption energies calculated as $\Delta E_{ads}^{H_2} = \Delta E_{des}^{\ddagger} - \Delta E_{ads}^{\ddagger}$, where $\Delta E_{des}^{\ddagger}$ values are based on the linear fit.

energies were calculated as $\Delta E_{ads}^{H_2} = \Delta E_{des}^{\ddagger} - \Delta E_{ads}^{\ddagger}$. We do not show measured values of $\Delta E_{des}^{\ddagger}$ at high x ($> \approx 0.8$) because their experimental uncertainties are large. For the calculation of $\Delta E_{ads}^{H_2}$ throughout composition space, we use a linear fit of the $\Delta E_{des}^{\ddagger}$ values measured at low x. At high concentrations of Cu, $\Delta E_{ads}^{H_2}$ appears constant at ~-0.3 eV (although the uncertainty here is large). As the amount of Pd in the alloy increases, $\Delta E_{ads}^{H_2}$ becomes increasingly negative, until $x \approx 0.6$, below which an increase in adsorption energy is observed.

3.2. Selection of the Active Site Basis Set. Our strategy for computing an effective dissociative adsorption energy is to compute the adsorption energies of a basis of active sites and then to average them in a suitably weighted way. The first step is identifying a basis of active sites on which to compute adsorption energies. The structure of the active sites is largely determined by the structure of the surface, which is in turn determined by the structure of the bulk. On the basis of the experimental phase diagram,[5,32] the CuPd system is in a disordered fcc bulk phase for the majority of the bulk composition space examined in this work; a B2 phase becomes stable for $0.51 < x < 0.68$ at 800 K, the temperature to which the CSAF was annealed during preparation. We neglect the B2 phase in this work. We expect that the fcc(111) orientation is predominant at the surface of the polycrystalline CSAF used in the experimental portion of this study.[19] Hence, we focus our modeling on the basis sites in an fcc(111) surface. Hydrogen adsorption energies were calculated on the fcc, hcp, bridge, and top sites of the pure component metals. The fcc adsorption site was found to be the most stable on each of the pure metal surfaces, and it is assumed that this will be the case for all alloy compositions, as well.

On the surface of an alloy, it is not clear what defines an adsorption site. A minimal site would be three atoms defining the fcc hollow position; however, there are ligand effects from atoms not directly adjacent to the adsorbate that influence the reactivity of those atoms. These effects tend to decay quickly with distance.[4] We seek a balance between the minimal number of atoms in a site that captures the dominant trends in activity but that are still enumerable. The minimum number of atoms needed to characterize an fcc site is three. For the fcc(111) surface of a CuPd alloy, this results in the four active sites shown in Figure 3. Only four sites are considered because rotations of the two mixed composition sites are assumed to have identical adsorption energies.
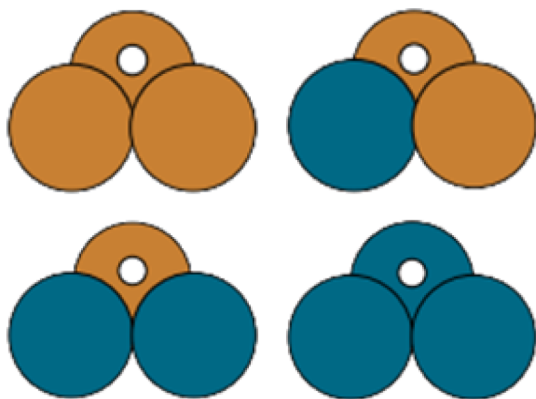

Figure 3. Four possible configurations of Cu (orange) and Pd (blue) atoms that can form fcc adsorption sites for hydrogen atoms.

These sites must be embedded into an alloy slab for the adsorption energy to be calculated. It is not computationally feasible to model all possible slab compositions. Rather than attempt to mimic the alloy slab, we chose to embed these sites into pure Cu slabs and pure Pd slabs. This will mimic ligand effects on the embedded sites and is likely to span the full range of these effects on the adsorption energies. Thus, we expect that this will provide bounds on the true adsorption energy for each site. This results in a total of eight unique slab compositions that were considered for the CuPd alloy portion of this study.

3.3. Active Site Adsorption Energies. The next objective is to estimate the adsorption energy of a site that is embedded in a slab with properties of a bulk alloy of a given composition, for example, at the lattice constant of the bulk alloy. We have to decide on the lattice constant that is appropriate for the calculation. In essence, we treat the slab as an effective medium that has an electronic structure similar to that of features that the alloy would have so that we can estimate the adsorption energy of a site in that alloy.

The lattice constant of many alloys is often a linear function of bulk composition (Vegard's law[33,34]). This trend maps the lattice constant to the bulk composition space as shown in eq 1:

$$\alpha(x) = (a_{Pd} - a_{Cu})x + a_{Cu} \tag{1}$$

where α is the alloy lattice constant, a_M is the lattice constant of pure component metal, M. We can readily verify this trend computationally using cluster expansion methods of the stable ground state configurations of the alloy.[35,36] The resulting ground state configurations from a cluster expansion of the CuPd system are shown in Figure 4. The lattice constants of
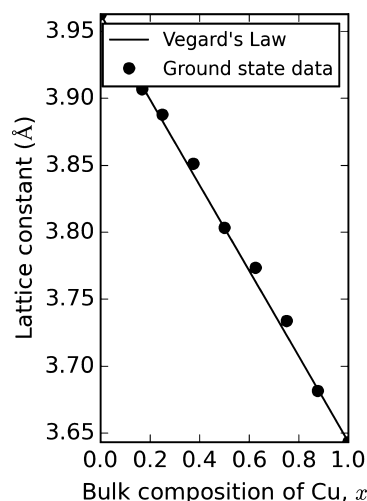

Figure 4. Lattice constants of the ground state fcc CuPd configurations plotted with Vegard's law as a function of bulk composition.

the ground state configurations vary linearly with alloy composition. This is in good agreement with Vegard's law. Thus, we use eq 1 to determine the slab lattice constant for any given bulk composition.

We can now calculate the adsorption energy on each site in our basis set as a function of bulk composition by defining the lattice constant of the slab. For the eight unique slab configurations, dissociative adsorption energies (ΔE_i) were calculated using eq 2.

$$\Delta E_i = E_{i,(\text{slab}+\text{H})} - E_{i,(\text{slab})} - \frac{1}{2}E_{(\text{H}_2)} \qquad (2)$$

where E_i represents the total energy of the slab with adsorbate, clean slab, and hydrogen molecule from left to right. i is an index for one of the eight slab configurations. Multiple adsorption energies, at various lattice constants, were calculated for each of these configurations and fitted to a second order polynomial equation of adsorption energy vs lattice constant (eq 3).

$$\Delta \tilde{E}_i(x) = A_i(\alpha(x))^2 + B_i(\alpha(x)) + C_i \qquad (3)$$

where A_i, B_i, and C_i are the fitting parameters of the adsorption energies calculated for configuration i. The lattice constant parameter defined in eq 1 can now be used to represent these continuous functions in terms of bulk composition.

Figure 5 shows the resulting ΔE_i calculated for each individual site embedded in a Cu slab and Pd slab as a
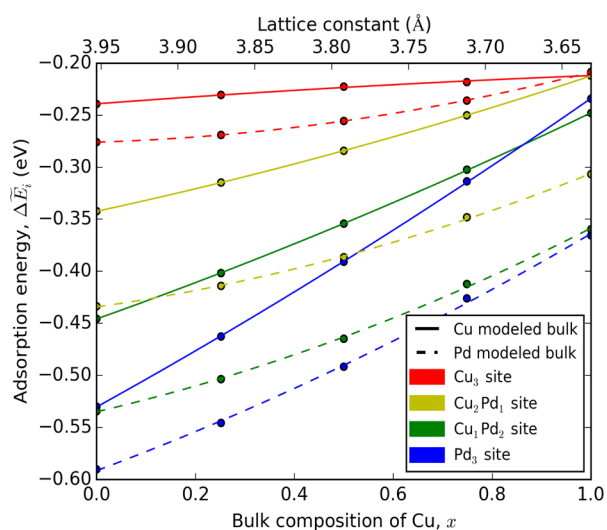

Figure 5. Adsorption energies for a H atom plotted against lattice constant and bulk composition. Solid lines represent models with Cu atoms in the subsurface layers, and dashed lines represent Pd subsurface atoms. Each color represents one of the surface configurations shown in Figure 3

function of lattice constant. The points were then fit using eq 3, resulting in the continuous functions shown as the solid and dashed lines.

Solid lines represent active sites embedded in a Cu slab; dashed lines represent sites in Pd. There is a notable difference between the energies of the two data sets, with more favorable adsorption for sites embedded in Pd. This difference is characteristic of the ligand effects and puts some bounds on the possible variations with composition. This effect is typically small (<0.05 eV) and results in a slight shift of adsorption energies across lattice constants, leaving the trends relatively unchanged. The results can be converted from a basis of lattice constant to bulk composition using eq 1 which is represented in the secondary x-axis of Figure 5.

3.4. Active Site Probabilities and Effective Adsorption. To determine the effective adsorption energy, we need the active site distribution. The probability of finding each of the four active sites is determined by the surface composition and its ordering. The CuPd system forms a disordered fcc bulk alloy, so we assume that the surface is also randomly ordered.

This means that the probability of finding a site is dictated by the composition of the site. Figure 6 shows this random
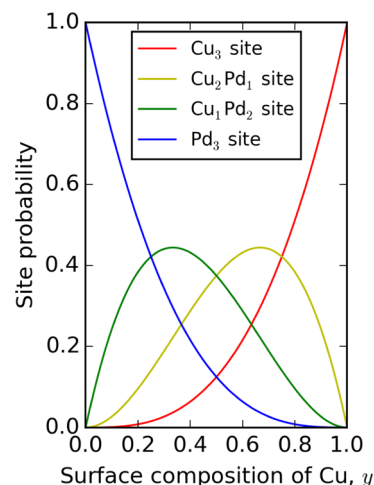

Figure 6. Fraction of active sites present on the clean surface of a CuPd alloy, assuming a perfectly random distribution of surface atoms.

distribution profile for the CuPd system as a function of surface composition. Similar statistical distributions have been calculated and compared to experimental observations for PdRu systems.[37] For PdRu, an increased concentration of pure component metal active sites is observed over mixed component sites. Deviations from the distributions shown in Figure 6 are the result of short-range ordering on the surface.

These distributions are based on arbitrary *surface* compositions and do not account for segregation effects. Because there are three possible configurations of the mixed composition sites, it becomes three times more likely to find them. Weighting the adsorption energies determined using eq 3 using the probabilities described above results in the effective adsorption energy ($\Delta \tilde{E}$) shown in eq 4.

$$\Delta \tilde{E}(x, y) = \sum_i R_i \, Pr_i(y) \, \Delta E_i(x) \qquad (4)$$

where R_i is the number of configurations identical to configuration i, Pr_i is the probability of slab configuration i, and y is the surface composition of Cu. In the absence of segregation, $y \approx x$, and this equation becomes a descriptor of the observed adsorption energy on the surface as a function of the bulk composition of the alloy. However, segregation will be negligible only for systems with similar parent metals and adsorbates that do not interact strongly with the surface. Because most systems of interest do not fit these criteria, we next develop a means of estimating the surface composition under reaction conditions.

3.5. Estimating Surface Composition under Reaction Conditions. Segregation is a phenomena that reduces the surface free energy of alloys. In vacuum, it is generally observed that the less reactive metal of an alloy segregates to the surface.[11,38] The Langmuir−McLean formulation of the Gibbs free isotherm (eq 5) relates the surface and bulk compositions of a binary alloy to the Gibbs free energy of segregation.[9]

$$\frac{y}{1 - y} = \frac{x}{1 - x} \exp\left(\frac{-\Delta G^{\text{seg}}}{k_B T}\right) \qquad (5)$$

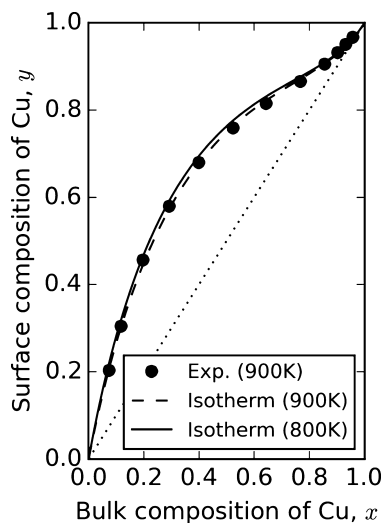Figure 7 shows the segregation profiles resulting from eq 5 at 800 and 900 K using the experimental segregation energies.[10]

Figure 7. Experimental surface segregation for CuPd alloy under ultrahigh-vacuum conditions. Black dots represent experimental measurements of top surface layer concentrations at 900 K using LEISS. The dashed line shows the Gibbs isotherm fit to the experimental data at 900 K using the segregation energies found in ref 10. The solid line shows the Gibbs isotherm using the same segregation energies at 800 K.

The data shown in this figure was collected using low energy ion scattering spectroscopy (LEISS) which samples only the top layer concentration of an alloy with a predetermined bulk composition. Figure 7 shows that under ultrahigh vacuum conditions the concentration of Cu at the topmost layer of the CuPd alloy will always be greater than the concentration in the bulk. This segregation is shown to increase as temperature drops until it reaches ≈ 700 K, below which the surface may not be at equilibrium with the bulk because of slow diffusion of metal atoms.[9]

In the presence of adsorbates, however, a strong adsorption bond to a more reactive metal may lead to segregation reversal. Both the vacuum and adsorbate-induced segregation can be lumped into a total Gibbs free energy of segregation under reaction conditions (eq 6).[6,39] The relevant segregation driving force for adsorption induced segregation is the difference in adsorption energy between the pure component metals. If adsorption is more favorable at one metal than the other, it provides a driving force for segregation. We approximate this driving force as the difference in adsorption energy on Cu(111) and Pd(111) times the coverage of adsorbates.

$$\Delta\tilde{G}(x, y) = \Delta G_{vac}^{seg}(x, y) + \theta_{H}(x, y)(\Delta E_{ads}^{Cu} - \Delta E_{ads}^{Pd}) \tag{6}$$

where $\Delta\tilde{G}$ is the total Gibbs free energy of segregation, ΔG_{vac}^{seg} is the Gibbs free energy of segregation in vacuum, ΔE_{ads}^{M} is the adsorption energy of pure metal M, and θ_{H} is the coverage of hydrogen atoms on the surface. ΔG_{vac}^{seg} is known from Figure 7. Under vacuum conditions or above the desorption temperature, θ_{H} goes to zero, and ΔG_{vac}^{seg} is recovered as the total segregation energy; likewise if the adsorption energy difference between the two metals goes to zero. It is important to note that this is the simplest possible formulation for the adsorbate induced contribution the segregation energy. It does not account for

strain effects of the differences of pure active sites at difference alloy bulk compositions, which have been discussed in other work.[40] This results in an over prediction of favorable adsorption onto the surface. A more detailed discussion of the incorporation of strain effects can be found in the Supporting Information file.

We solve for θ_{H} using a simple Langmuir isotherm for dissociative adsorption of hydrogen onto the surface of the alloy.[41] The isotherm is dependent upon adsorption energy for each individual adsorption site. These are estimated as a function of bulk composition, as shown previously in Figure 3. Here, it is assumed that the dissociative adsorption energy on each site is independent of coverage. The coverage on an individual site i can then be expressed as shown in eq 7.

$$\theta_{i}(x) = \frac{\sqrt{\exp\left(\frac{-\Delta E_{i}(x)}{k_{B}T}\right)P_{H_{2}}}}{1 + \sqrt{\exp\left(\frac{-\Delta E_{i}(x)}{k_{B}T}\right)P_{H_{2}}}} \tag{7}$$

where θ_{i} is the hydrogen coverage contribution from site i, and $P_{H_{2}}$ is the pressure of hydrogen gas. The total coverage of hydrogen on the surface of the alloy can then be obtained by summing the coverage on each site multiplied by the site probability, that is, $\theta_{H}(x, y) = \sum_{i} R_{i} Pr_{i}(y) \theta_{i}(x)$. The total segregation energy can then be reformulated as a function of the bulk and surface composition of the alloy, as shown in eq 8.

$$\Delta\tilde{G}(x, y) = -k_{B}T \ln\left(\frac{y(1 - x)}{x(1 - y)}\right)$$
$$= \Delta H_{vac}^{seg}(x) - T\Delta S_{vac}^{seg}(x) + \theta_{H}(x, y)$$
$$(\Delta\tilde{E}(1, 1) - \Delta\tilde{E}(0, 0)) \tag{8}$$

Inserting eq 8 into eq 5 leads to a single equation with a single unknown: the surface composition. This function then depends only on the bulk composition, the reaction conditions, the adsorption energies on each site, and the site distribution. We assume the adsorption energies are independent of coverage. At higher coverages than 0.25 ML, the adsorption energies may increase (become less stable) by up to 0.05−0.1 eV, depending on the metal. Figure 8 shows the predicted surface composition under reaction conditions for the CuPd system, which results from the solution to eq 8. The segregation profiles shown represent the adsorbate-induced surface composition of the alloy. We performed the analysis for sites embedded in a Cu slab (solid) and Pd slab (dashed). The difference between the two profiles places bounds on our estimates.

Comparison of Figures 7 and 8 clearly indicates that the surface composition under reaction conditions is markedly different than in vacuum. This is a result of preferential bonding between hydrogen and adsorption site configurations which contain high concentrations of Pd, resulting in a substantial increase of Pd at the surface under reaction conditions.

The effective hydrogen adsorption energies that are consistent with segregation for the CuPd systems and a comparison to the experimental results are included in Figure 9. The solid blue line represents the effective adsorption energies predicted for the four surface configurations embedded in a Cu slab and the dashed line for the sites embedded in a Pd slab. Both sets of data show similar trends, with weaker adsorption energies on Cu-rich surfaces than on Pd-rich surfaces. The sites embedded in the Pd slab are more consistent with the
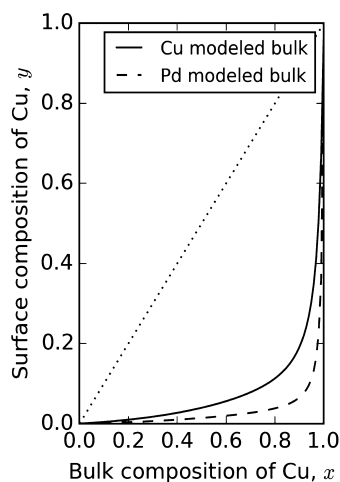
Figure 8. Segregation profile of the CuPd system at 800 K and 1 atm of hydrogen. The solid line represents the predicted surface concentrations for active sites modeled on Cu subsurface layers and the dashed line for Pd subsurface layers.
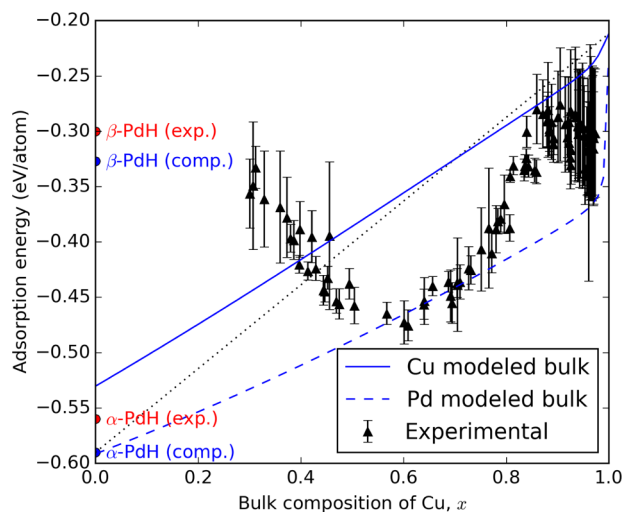

Figure 9. Effective hydrogen adsorption energies on Cu_xPd_{1-x} alloys modeled using adsorption site configurations embedded in bulk Cu (solid line) and Pd (dashed line) as a function of bulk alloy composition for an fcc(111) surface. The dotted black line represents a linear trend between adsorption energies of pure component metals. Black triangles represent experimental data shown in Figure 2 with corresponding experimental uncertainty. The experimentally determined adsorption energies for the α- and β-Pd hydride phases are also shown in red.

experimental results, indicating that Pd–ligand effects are probably significant in determining the actual site reactivities.

The dotted black line represents the linear average between the adsorption energies of the pure component metals. From Figure 9, it can be seen that the experimental data are not well characterized by the adsorption energy of a single active site (a horizontal line) or the linear interpolation between the adsorption energy of the pure component metals. This is characteristic of segregation effects on the surface of the alloy, resulting in more favorable active sites at the surface under reaction conditions. This is supported by the fact that the effective adsorption calculated without segregation effects does not accurately predict the experimental adsorption trend either.

Effective adsorption energy predictions without segregation effects can be found in the Supporting Information file.

Predicted and experimental composition-dependent adsorption energies are in good agreement for $x > 0.5$. The deviation of experimental data away from the bounded region at $x < 0.4$ is possibly due to the formation of a dense hydride phase whose reactivity is different from the metallic surfaces modeled in this work. There are two PdH phases: the α-phase, which has a very low H concentration, and β-phase, which forms a rock salt structure.[42] Because of the low concentration of H in the α-phase, it is expected that the hydrogen adsorption energy will be quite similar to that on a pure Pd fcc configuration, such as the one incorporated into our model. The experimentally measured adsorption energy for the α-PdH phase is -0.56 eV/atom,[18] which falls well within the predicted bounds of effective adsorption using our method, as shown in Figure 9. The experimental adsorption energy for the β-PdH phase was measured at -0.3 eV/atom.[18] Calculations were performed on both the fcc and hcp active sites of a Pd-terminated stoichiometrically equivalent β-PdH. The adsorption energies were determined to be -0.327 and -0.283 eV/atom for the hcp and fcc active sites, respectively. The energy for the more favorable hcp site is in good agreement with the experimental result of -0.3 eV/atom. The observed trend in experimental adsorption energies on the CuPd CSAF appears to be moving toward this higher energy, suggesting the formation of the β-hydride phase.

4. CONCLUSIONS

We have shown that the reactivity of a CuPd alloy for H_2–D_2 exchange cannot be explained simply by a single site, nor as a simple linear average of the pure metal components. The reactivity is determined by the distribution of active sites, which depends on the surface composition. The surface composition, in turn, depends on the bulk composition *and* the reaction conditions.

In this work, we developed a methodology to estimate the reactivity of an alloy surface that takes these factors into account. We began by utilizing a basis set of active sites which spans the properties of the surface. Using DFT, we estimated the reactivity of each site by embedding the sites in metal slabs with geometric properties similar to a bulk alloy. Site distributions as a function of an arbitrary surface composition were estimated statistically. Finally, we solved for the surface composition by balancing vacuum and adsorbate induced segregation energies through the Langmuir–McLean formulation of the Gibbs isotherm.

Using this methodology, we estimated the dissociative adsorption energy of hydrogen on CuPd surfaces as a function of the bulk composition. In parallel, we measured the adsorption energy of hydrogen on a composition spread alloy film. This method was found to give good agreement with experimental adsorption energies for the CuPd system in the Cu rich region, falling within predicted bounds of ≈ 0.08 eV range at $x > 0.5$. Below this range, there is poor agreement with experimental results, which is possibly due to the formation of a hydrogen rich β-PdH phase.

■ ASSOCIATED CONTENT

⑤ Supporting Information

The following file is available free of charge on the ACS Publications website at DOI: 10.1021/cs501585k.

Full details of the calculations and analysis (PDF)

■ AUTHOR INFORMATION

Corresponding Author
*E-mail: jkitchin@andrew.cmu.edu.

Notes

The authors declare no competing financial interest.

■ ACKNOWLEDGMENTS

■ REFERENCES

(1) Yu, W.; Porosoff, M. D.; Chen, J. G. *Chem. Rev.* **2012**, *112*, 5780−5817.
(2) Kitchin, J. R.; Miller, S. D.; Sholl, D. S. *Chemical Modelling: Applications and Theory*; The Royal Society of Chemistry, 2008; Vol. 5; pp 150−181.
(3) Greeley, J.; Nørskov, J. K. *Surf. Sci.* **2005**, *592*, 104−111.
(4) İnoğlu, N.; Kitchin, J. R. *Mol. Sim.* **2010**, *36*, 633−638.
(5) Dowben, P. A.; Miller, A. *Surface Segregation Phenomena*, 1st ed.; CRC Press: Boca Raton, FL, 1990.
(6) Kitchin, J. R.; Reuter, K.; Scheffler, M. *Phys. Rev. B* **2008**, *77*, 075437.
(7) Alfonso, D. R.; Cugini, A. V.; Sholl, D. S. *Surf. Sci.* **2003**, *546*, 12−26.
(8) Greeley, J.; Nørskov, J. K. *J. Phys. Chem. C* **2009**, *113*, 4932−4939.
(9) Miller, J. B.; Matranga, C.; Gellman, A. J. *Surf. Sci.* **2008**, *602*, 375−382.
(10) Priyadarshini, D.; Kondratyuk, P.; Picard, Y. N.; Morreale, B. D.; Gellman, A. J.; Miller, J. B. *J. Phys. Chem. C* **2011**, *115*, 10155−10163.
(11) Ruban, A.; Skriver, H.; Nørskov, J. *Phys. Rev. B* **1999**, *59*, 15990−16000.
(12) Han, J. W.; Kitchin, J. R.; Sholl, D. S. *J. Chem. Phys.* **2009**, *130*, 124710.
(13) Menning, C. A.; Chen, J. G. *J. Chem. Phys.* **2009**, *130*, 174709.
(14) Kim, H. Y.; Henkelman, G. *ACS Catal.* **2013**, *3*, 2541−2546.
(15) Han, B. C.; Van der Ven, A.; Ceder, G.; Hwang, B.-J. *Phys. Rev. B* **2005**, *72*, 205409.
(16) Mei, D.; Neurock, M.; Smith, C. M. *J. Catal.* **2009**, *268*, 181−195.
(17) Kamakoti, P.; Morreale, B. D.; Ciocco, M. V.; Howard, B. H.; Killmeyer, R. P.; Cugini, A. V.; Sholl, D. S. *Science* **2005**, *307*, 569−573.
(18) O'Brien, C. P.; Miller, J. B.; Morreale, B. D.; Gellman, A. J. *J. Phys. Chem. C* **2011**, *115*, 24221−24230.
(19) O'Brien, C. P.; Miller, J. B.; Morreale, B. D.; Gellman, A. J. *J. Phys. Chem. C* **2012**, *116*, 17657−17667.
(20) Fleutot, B.; Miller, J. B.; Gellman, A. J. *J. Vac. Sci. Technol. A* **2012**, *30*, 061551.
(21) Gumuslu, G.; Kondratyuk, P.; Boes, J.; Morreale, B.; Miller, J. B.; Kitchin, J.; Gellman, A. J. *Personal communications*, 2014
(22) Priyadarshini, D.; Kondratyuk, P.; Miller, J. B.; Gellman, A. J. *J. Vac. Sci. Technol. A* **2012**, *30*, 011503.
(23) Kondratyuk, P.; Gumuslu, G.; Shukla, S.; Miller, J. B.; Morreale, B. D.; Gellman, A. J. *J. Catal.* **2013**, *300*, 55−62.
(24) Kresse, G.; Furthmüller, J. *Phys. Rev. B* **1996**, *54*, 11169−11186.
(25) Kresse, G.; Furthmüller, J. *Comput. Mater. Sci.* **1996**, *6*, 15−50.
(26) Perdew, J. P.; Burke, K.; Ernzerhof, M. *Phys. Rev. Lett.* **1996**, *77*, 3865−3868.
(27) Perdew, J. P.; Burke, K.; Ernzerhof, M. *Phys. Rev. Lett.* **1997**, *78*, 1396−1396.
(28) Blöchl, P. E. *Phys. Rev. B* **1994**, *50*, 17953−17979.
(29) Kresse, G.; Joubert, D. *Phys. Rev. B* **1999**, *59*, 1758−1775.
(30) Monkhorst, H. J.; Pack, J. D. *Phys. Rev. B* **1976**, *13*, 5188−5192.
(31) Methfessel, M.; Paxton, A. T. *Phys. Rev. B* **1989**, *40*, 3616−3621.
(32) Subramanian, P. R.; Laughlin, D. E. *J. Phase Equilib.* **1991**, *12*, 231−243.
(33) Denton, A. R.; Ashcroft, N. W. *Phys. Rev. A* **1991**, *43*, 3161−3164.
(34) Bose, S. K.; Kudrnovský, J.; Jepsen, O.; Andersen, O. K. *Phys. Rev. B* **1992**, *45*, 8272−8282.
(35) van de Walle, A.; Asta, M. *Model. Simul. Mater. Sci. Eng.* **2002**, *10*, 521.
(36) van de Walle, A.; Ceder, G. *J. Phase Equilib.* **2002**, *23*, 348−359.
(37) Hartmann, H.; Diemant, T.; Bergbreiter, A.; Bansmann, J.; Hoster, H.; Behm, R. *Surf. Sci.* **2009**, *603*, 1439−1455.
(38) Ruban, A. V.; Simak, S. I.; Korzhavyi, P. A.; Johansson, B. *Phys. Rev. B* **2007**, *75*, 054113.
(39) Miller, J. B.; Morreale, B. D.; Gellman, A. J. *Surf. Sci.* **2008**, *602*, 1819−1825.
(40) Roudgar, A.; Groß, A. *Surf. Sci.* **2005**, *597*, 42−50.
(41) Miller, J. B.; Priyadarshini, D.; Gellman, A. J. *Surf. Sci.* **2012**, *606*, 1520−1526.
(42) Manchester, F. D.; San-Martin, A.; Pitre, J. M. *J. Phase Equilib.* **1994**, *15*, 62−83.